

# Exploiting Redundancy for Autonomous Calibration of a Planar Robot

Arthur E. Quaid and Alfred A. Rizzi  
Carnegie Mellon University  
Pittsburgh, Pennsylvania, USA  
{aquaid,arizzi}@ri.cmu.edu

**Abstract:** Autonomous calibration techniques are applied to the calibration of two sensors of a planar robot: a platen sensor and a coordination sensor. The redundant angle measurements of the platen sensor are used to identify its parameters, improving its output accuracy by better than a factor of two. Redundant position measurements using both sensors are also used in an attempt to further improve the platen sensor accuracy and identify the relative position of the two sensors.

## 1. Introduction

In the Microdynamic Systems Laboratory<sup>1</sup> at Carnegie Mellon University, we are developing modular robotic components and tools to support the rapid deployment and programming of high-precision automated assembly systems [1]. The overall goal is to provide mechanically, computationally, and algorithmically modular factory *agents* and a collection of tools to support a user's interaction with the agents in an effort to expedite the process of designing, integrating, and deploying automated assembly systems. The work presented here focuses on the calibration of one of the most basic components of this larger system – the sensor systems associated with *courier* agents.

A *courier* (shown schematically in Fig. 1) is a planar robot which serves as both a product-carrier and local manipulation device in a minifactory assembly system [1]. The device is built upon existing planar linear (Sawyer) motor technology [2], in which four linear stepping motors are combined in a housing to provide large  $x, y$  motions over a tabletop *platen* surface, as well as a rotation capability of a few degrees. Closed-loop control of these devices recently became possible with the development of a magnetic *platen sensor* [3]. This sensor detects the toothed structure of the platen surface and can interpolate between the nominal 1 mm tooth pitch to roughly 1 part in 5000, yielding an overall position sensing resolution of  $0.2 \mu\text{m}$ . The complete sensor (see Fig. 2) consists of four quadrature-pairs, shown schematically in Fig. 3. Each pair measures motion along one of the two cardinal directions by monitoring changes in the magnetic coupling between the drive and sense coils. When integrated, information from the four pairs allows measurement of the full 3-DOF position of the robot. In addition, the planar robot is augmented with a *coordination sensor*, shown in Fig. 4, based on an upward-facing lateral

---

<sup>1</sup>See <http://www.cs.cmu.edu/~msl>

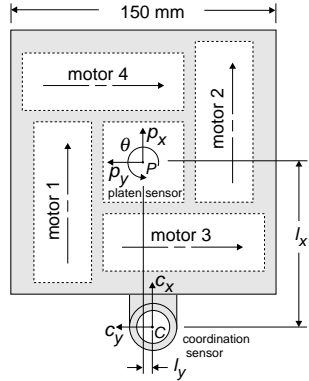


Figure 1. Courier top view

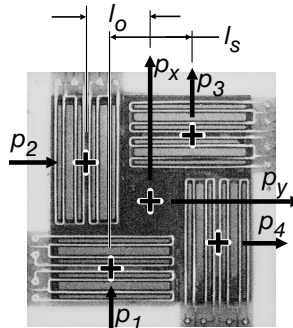


Figure 2. Platen sensor detail

effect position sensing diode. This device can precisely measure the relative displacement between the courier and overhead devices outfitted with LED beacons to sub-micron resolution [4].

Whereas basic models of planar linear motor sensors and actuators are sufficient for undemanding positioning applications, improved models are crucial for high-performance closed-loop operation. Poorly modeled effects including magnetic saturation, eddy-current damping, and non-linear position and angle dependencies limit positioning accuracies, controller robustness, and accurate force generation capabilities, all of which are vital for successful use in an environment such as the minifactory. Unfortunately, global effects such as platen tooth variations and thermal deformations are not easily captured by practical models, fundamentally limiting the accuracy of the models considered here.

Prior work in our laboratory has developed parameterized models for both the actuators and sensors by recourse to complicated and time-consuming processes which rely on high-precision independent sensors, specifically a laser interferometer and load cell [5, 3]. Realizing that model parameters will inevitably vary from device to device, and recognizing the need for stand-alone self-calibrating devices, a more practical procedure is necessary to support the autonomous calibration of individual devices in the field.

Fortunately, it has been shown that external measuring devices are not always necessary to accomplish such parameter identification tasks. Identification of the kinematic parameters of redundant manipulator systems can be performed by recording the joint angles during self-motions with the end-effector fixed in the workspace [6]. This technique has also been used for calibration of parallel mechanisms with redundant sensing [7]. Similarly, two 6-DOF force sensors pressing against each other in different configurations have been shown to provide sufficient information to enable their calibration [8]. The lesson to be taken from these works is that redundant measurements, even if individually inaccurate, can allow for autonomous calibration. In this paper, we focus on the application of these techniques to the calibration of the redundant sensors of the planar robot and experimentally demonstrate their effectiveness.

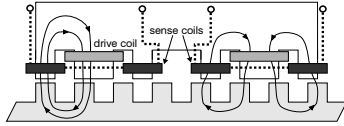


Figure 3. Schematic of a single platen sensor segment

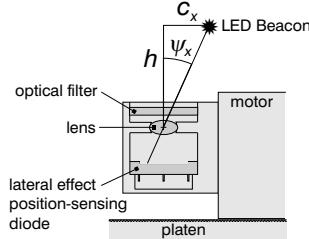


Figure 4. Coordination sensor

## 2. Approach

In general, the autonomous calibration methods mentioned above presume the existence of a parametric model for each sensing component of the form

$$y_i = f_i(k_i, u), \quad (1)$$

where  $y_i$  is the scalar sensor output,  $k_i \in \mathbb{R}^r$  is the vector of model parameters, and  $u \in \mathbb{R}^n$  is the vector of input variables. Given a set of these models,  $i \in \{1 \dots N\}$  with  $N > n$ , the redundancy of the sensor system can be expressed through a constraint equation,  $g(\cdot \cdot \cdot)$ , of the form

$$g(y_1(k_1, u), y_2(k_2, u), \dots, y_n(k_N, u)) = 0. \quad (2)$$

The task is to recover the parameter vectors,  $k_i$ , given a series of measurements of the input vectors,  $u_j$   $j \in \{1 \dots M\}$ . This is, in general, a non-linear optimization or root-finding problem and iterative methods are traditionally used to minimize  $\sum_{j=1}^M g_j^2$  over the parameter vectors,  $k_1 \dots k_N$ . However, if the models,  $f_i(\cdot \cdot \cdot)$ , are linear in the parameter vectors and the constraint equation,  $g(\cdot \cdot \cdot)$ , is linear in the outputs,  $y_i$ , it is well known that an analytic closed-form solution can be found.

The following section presents our application of these ideas to the autonomous calibration of both the platen and coordination sensor for a courier robot. To quantitatively evaluate and understand the benefit of including multiple sensing modalities, we have applied a number of different verification methods to these experiments. These include examining the condition number of the second derivatives of  $\sum_j g_j^2$  (which provides evidence for the identifiability of the parameters), and the magnitude of the residual error both over the calibration data and independent test data. While these methods can detect a number of deficiencies, they are insensitive to certain model defects or violations of assumptions. These defects can often be detected through the use of an external sensor, and thus we also include comparisons against an independent sensor whenever possible.

## 3. Results

In this section, autonomous calibration of the platen sensor using a linear constraint equation is first presented. The platen sensor error model is then extended to include additional effects, and nonlinear constraint equations are de-

rived to simultaneously calibrate the platen sensor parameters and the mounting parameters of the coordination sensor.

### 3.1. Platen sensor autonomous calibration

#### 3.1.1. Formulation

Prior work [3] used a cumbersome but highly-precise laser interferometer to calibrate the platen sensor error. Fourier techniques were used to identify the significant frequency components of the error (difference from an idealized sensor model) as a function of the courier position. This demonstrated that the error of each sensor segment is well-modeled by an equation of the form

$$e_i := \begin{aligned} &k_{i,0} + k_{i,1} \sin(f\bar{p}_i) + k_{i,2} \cos(f\bar{p}_i) + k_{i,3} \sin(2f\bar{p}_i) + k_{i,4} \cos(2f\bar{p}_i) + \\ &k_{i,5} \sin(4f\bar{p}_i) + k_{i,6} \cos(4f\bar{p}_i) + k_{i,7} \sin(6f\bar{p}_i) + k_{i,8} \cos(6f\bar{p}_i), \end{aligned} \quad (3)$$

where  $\bar{p}_i$  is the unmodified output of the  $i^{\text{th}}$  sensor,  $f := 2\pi/\rho$ , and  $\rho$  is the pitch of the sensor teeth – 1.016 mm for our device. This model assumes the error is small enough that  $\bar{p}_i$  can be used instead of the actual positions  $p_i^*$  – *i.e.* the relation between the “measured position,”  $\bar{p}_i$ , and the actual position,  $p_i^*$ , is monotonic. Effects of the courier angle,  $\theta$ , on the output are similarly neglected. As a result of these assumptions, the error,  $e_i$ , is linearly related to the parameter vector  $k_i := [k_{i,0}, \dots, k_{i,8}]^T$  and can be written as  $e_i = \Gamma_i^T k_i$ , where  $\Gamma_i$  is a vector of sine and cosine terms. Neglecting noise and unmodeled effects, the calibrated sensor output can be written as  $\hat{p}_i := \bar{p}_i + e_i$ . The *sensor segment pair* in either cardinal direction can then be used to independently compute the angle of the courier:

$$\hat{\theta}_x := \frac{\hat{p}_1 - \hat{p}_3}{l_s} \quad \text{and} \quad \hat{\theta}_y := \frac{\hat{p}_2 - \hat{p}_4}{l_s}, \quad (4)$$

where  $l_s$  is the distance between sensors (9.7 mm), as shown in Fig. 3. In normal operation, the angles in (4) are averaged to reduce measurement noise, but here their redundancy is used to form a constraint equation,

$$\begin{aligned} g_p &= (\hat{\theta}_x - \hat{\theta}_y)l_s \\ &= (\hat{p}_1 - \hat{p}_3) - (\hat{p}_2 - \hat{p}_4). \end{aligned} \quad (5)$$

Given a set of  $M$  observations,  $\bar{p}_{i,j}$ , indexed by  $j \in \{1, \dots, M\}$ , we construct the overall cost  $\sum_{j=1}^M (g_{p,j})^2$  and find the set of parameters,  $k_i$ , which minimize it. Here, the constraint is linear in the parameters and a closed-form solution exists. Defining the constraint error for a single observation as

$$\tilde{g}_{p_j} := (\bar{p}_{1,j} - \bar{p}_{3,j}) - (\bar{p}_{2,j} - \bar{p}_{4,j}) \quad (6)$$

we can rewrite (5) as  $g_{p_j} = \tilde{g}_{p_j} + (e_{1,j} - e_{3,j}) - (e_{2,j} - e_{4,j})$ . Making explicit the linear dependence of (3) on  $k_i$  yields

$$g_{p_j} = \tilde{g}_{p_j} + \sum_i \Gamma_{i,j}^T k_i = \tilde{g}_{p_j} + \Gamma_j k, \quad (7)$$

where  $\Gamma_j$  and  $k$  combine the  $\Gamma_{i,j}$  and  $k_i$  into single vectors. This form directly admits a linear least squares solution. Collecting the data over the index  $j$

leads to  $G_p = \tilde{G}_p + \Gamma k$ , with  $G_p := [g_{p1}, \dots, g_{pM}]^T$ ,  $\tilde{G}_p := [\tilde{g}_{p1}, \dots, \tilde{g}_{pM}]^T$ , and  $\Gamma := [\Gamma_1, \dots, \Gamma_M]^T$ . The optimal parameter set is then given by

$$k = \Gamma^\dagger \tilde{G}_p, \quad (8)$$

where  $\Gamma^\dagger$  is the pseudo-inverse of  $\Gamma$ .

### 3.1.2. Experiments

For this and later experiments, the quality of calibration is evaluated by examining the *residual error* vector, computed from the errors in the relevant constraint equation over the dataset, and also by examining the *position error* and *angle error* vectors, computed by comparing the calibrated platen sensor outputs to laser interferometer ground truth measurements for each datapoint. These errors are reported for the calibrated and uncalibrated sensor for comparison purposes, and error magnitudes are reported in terms of the standard deviation of the error vector elements.

Using an open-loop controller, the courier was moved to a series of uniformly distributed random  $(x, y, \theta)$  positions over a range of  $0 < x, y < 10\rho$  and  $-0.5^\circ < \theta < 0.5^\circ$ . The output of the data collection routine consisted of a vector of platen sensor outputs for each of 1000 courier positions.

Using this dataset,  $\Gamma$  and  $\tilde{G}_p$  were constructed from  $\tilde{p}$  using the method described in Sec. 3.1.1. To confirm the identifiability of  $k$ , the condition number of  $\Gamma$  was computed and found to be small<sup>2</sup> (about 8) suggesting that the parameters were sufficiently excited by the data. The impact of the remaining unmodeled effects was computed by evaluating the residual error,  $r := \Gamma k - \tilde{G}_p$ . Using the identified parameters, the residual was  $4.1 \mu\text{m}$ , significantly smaller than the  $29.3 \mu\text{m}$  residual using a zero vector for  $k$ , but still higher than the sub-micron resolution of the sensor.

To examine the generality of  $k$ , the courier was commanded to move a distance of 40 mm passing through the calibration area. For this *fly-by* test, the residual decreased from  $12.1 \mu\text{m}$  to  $5.5 \mu\text{m}$  with calibration, indicating that  $k$  was also valid over this dataset. To provide an independent verification and better characterize the performance of the autonomous calibration, retroreflectors were mounted on the courier, allowing a laser interferometer to precisely measure two axes. The 40 mm fly-by test was repeated, and the translation along the direction of motion and rotation in the plane were sampled by both the interferometer and platen sensor. Using the interferometer measurements as ground-truth, the sensor translation errors are shown in Fig. 5 and the errors for each of the sensor angle measurements are shown in Fig. 6. The position error decreased from  $8.9 \mu\text{m}$  to  $6.5 \mu\text{m}$  with calibration. The error of  $\theta_x$  stayed about the same at 0.4 mrad, while the error of  $\theta_y$  decreased from 1.2 mrad to 0.4 mrad with calibration.

Although the autonomous calibration does yield a nominal improvement in position error and an improvement in the  $\theta_y$  angle error by a factor of 3, there is a significant systematic error in  $\theta_x$  that does not decrease. For this test, the courier moves in the  $y$  direction, nominally leaving fixed the outputs

---

<sup>2</sup>As the arbitrary offset parameters  $k_{i,0}$  cannot be individually identified, the condition number computation considered only their sum.

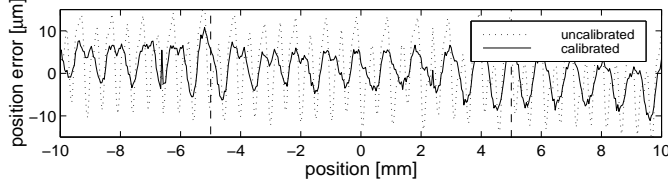


Figure 5. Position error in direction of motion during motion through platen sensor calibration region (indicated by dashed lines).

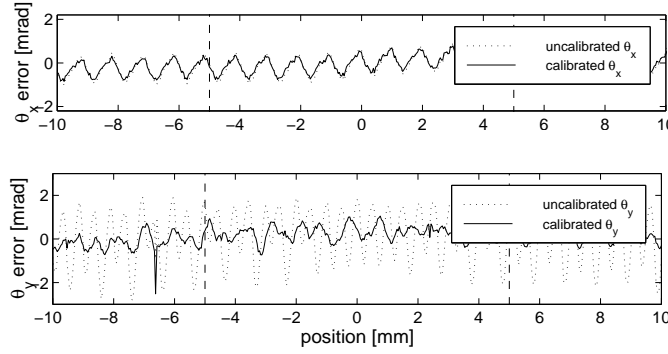


Figure 6. Angle error during motion through platen sensor calibration region.

of the sensors that measure motion in the  $x$  direction, which are also used to compute  $\theta_x$ . Errors in  $\theta_x$  are therefore best explained as an unmodeled dependence of the output on lateral position. As these *lateral dependencies* are roughly the same size as the residual errors and are unmodeled by (3), they are likely to be limiting further error reduction. However, the structure of the constraint equation (5) makes it difficult to distinguish lateral dependencies of one sensor segment pair from translational effects of the perpendicular sensor segment pair.

### 3.2. Dual sensor autonomous calibration

In hopes of identifying these lateral effects, the coordination sensor can be used to provide additional constraints. However, the precise mounting position and other parameters of the coordination sensor are not known. In this section, the autonomous calibration method is applied to the calibration of both the coordination sensor and an extended model of the platen sensor.

To model the lateral motion effects, the platen sensor models are augmented with additional parameters based on their lateral motion

$$\begin{aligned}
 e'_1 &= e_1 + k_{1,9} \sin(f(\bar{p}_y - l_o \bar{\theta})) + k_{1,10} \cos(f(\bar{p}_y - l_o \bar{\theta})) \\
 e'_2 &= e_2 + k_{2,9} \sin(f(\bar{p}_x + l_o \bar{\theta})) + k_{2,10} \cos(f(\bar{p}_x + l_o \bar{\theta})) \\
 e'_3 &= e_3 + k_{3,9} \sin(f(\bar{p}_y + l_o \bar{\theta})) + k_{3,10} \cos(f(\bar{p}_y + l_o \bar{\theta})) \\
 e'_4 &= e_4 + k_{4,9} \sin(f(\bar{p}_x - l_o \bar{\theta})) + k_{4,10} \cos(f(\bar{p}_x - l_o \bar{\theta})),
 \end{aligned} \tag{9}$$

where  $\bar{p}_x = (\bar{p}_1 + \bar{p}_3)/2$  and  $\bar{p}_y = (\bar{p}_2 + \bar{p}_4)/2$  are the average of the uncalibrated

sensor readings along each axis, and  $\bar{\theta}$  is the average of the uncalibrated angle measurements computed as in (4). The error of each sensor segment is now dependent on the measurements of the other segments.

Although the coordination sensor requires internal calibration for electronic gains, mounting inaccuracies, optical distortions, and PSD nonlinearities, we assume for now that these effects have been calibrated<sup>3</sup> so that it outputs a perfect measurement of the angles to the LED beacon ( $\psi_x$  and  $\psi_y$ ). Assuming a stationary beacon, the motion of the sensor is given by

$$c_x = h \tan(\psi_x) \quad \text{and} \quad c_y = h \tan(\psi_y). \quad (10)$$

As the coordination sensor supplies two additional measurements, two more constraint equations can be derived. A physically meaningful constraint is to equate the displacements of coordination sensor ( $c_x, c_y$ ) with that of the platen sensor ( $p_x, p_y$ )

$$\begin{bmatrix} g_x \\ g_y \end{bmatrix} = \begin{bmatrix} -\hat{p}_x + \cos(\hat{\theta})c_x - \sin(\hat{\theta})c_y - l_y \sin(\hat{\theta}) + l_x \cos(\hat{\theta}) + o'_x \\ -\hat{p}_y + \sin(\hat{\theta})c_x + \cos(\hat{\theta})c_y + l_y \cos(\hat{\theta}) + l_x \sin(\hat{\theta}) + o'_y \end{bmatrix}, \quad (11)$$

where  $c_x, c_y$  are relative to coordinate frame  $C$  shown in Fig. 1, which has a stationary origin under the LED beacon but rotates with  $\theta$ . The platen sensor positions  $\hat{p}_{x,y}$  are relative to stationary coordinate frame  $P$ , and are simply the average of the two platen sensor measurements in each direction. Parameters  $l_x$  and  $l_y$  are the physical offsets between the centers of the two sensors as measured on the body of the courier, while offsets  $o_x$  and  $o_y$  account for the arbitrary zero position of the platen sensor. The angle of the courier,  $\hat{\theta}$ , is the average of  $\hat{\theta}_x$  and  $\hat{\theta}_y$  in (4).

These constraint equations contain five new parameters to be identified ( $h, l_x, l_y, o_x, o_y$ ), in addition to the platen sensor parameters ( $k_1, k_2, k_3, k_4$ ). The three constraint equations  $g_x, g_y$ , and  $g_p$  are combined by taking the sum of their squares to provide a scalar valued function for minimization.

### 3.2.1. Experiments

The courier was positioned so that the coordination sensor was directly under an LED beacon and was moved to a series of uniformly distributed random  $(x, y, \theta)$  positions over a range of  $0 < x, y < 2\rho$  and  $-1.5^\circ < \theta < 1.5^\circ$ . In this case, courier rotation was about the center of the coordination sensor in order to minimize the effects of coordination sensor nonlinearities. The output of this data collection process consisted of a vector of platen sensor outputs,  $\bar{p}$ , and coordination sensor outputs,  $(\psi_x, \psi_y)$ , for each of 1000 courier positions.

Using this dataset, a cost function  $J = \sum_j (g_{x,j}^2 + g_{y,j}^2 + g_{p,j}^2)$  was computed using the procedure described above. As the constraint equations are non-linear in the parameters, definitive testing for identifiability of parameters is difficult. The condition number of a numerically computed linear approximation of the second derivative of  $J$  was examined at both the initial parameter and the calibrated parameter results, and was very large at both ( $8.11 \times 10^8$  and  $3.38 \times 10^8$  respectively). The largest singular value was also large (at least  $5 \times 10^4$

<sup>3</sup>In practice these parameters would be identified prior to integration with the courier.

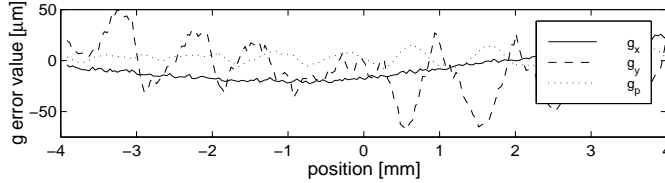


Figure 7. Constraint equation errors during motion through dual sensor calibration region.

for both cases), suggesting a stiff system rather than completely unidentifiable parameters. To investigate further, a synthetic data set was generated using nominal parameter values and Gaussian noise added to the sensor outputs. The cost function,  $J$ , was used with a BFGS Quasi-Newton method with a mixed quadratic and cubic line search procedure<sup>4</sup> and identified the correct parameters to within  $20 \mu\text{m}$  for  $h, l_x$ , and  $l_y$ , and within a micron for the remaining parameters, even with initial errors of 5% for the coordination sensor parameters,  $3 \mu\text{m}$  random errors in the platen sensor parameters, and all sensor readings corrupted by  $1.0 \mu\text{m}$  standard deviation Gaussian noise.

Encouraged by the simulation results, the same cost function and minimization routine were applied to the experimental dataset. To provide a good initial parameter vector, the platen sensor autonomous calibration results were used to initialize the basic set of platen sensor parameters, while the coordination sensor parameters ( $o_x, o_y, l_x, l_y, h$ ) were initialized by minimizing a partial cost function  $J' = \sum_j (g_{x,j}^2 + g_{y,j}^2)$  with the platen sensor parameters fixed. With these initial parameter estimates, the complete cost,  $J$ , was minimized over the full set of parameters, including the lateral effect terms ( $k_{i,9}, k_{i,10}$ ). The residuals of the three constraints ( $g_x, g_y, g_p$ ) were computed at the initial and final parameter vectors, with values  $(8.4, 31.6, 4.2) \mu\text{m}$  and  $(8.06, 25.2, 5.19) \mu\text{m}$ , respectively. The main change is a decrease in  $g_y$ , which includes the large lever-arm term  $l_x \sin(\theta)$  (with  $l_x \approx 90 \text{ mm}$ ) and is very sensitive to the angle error of the platen sensor. To test the calibration over a different dataset, residuals for the three constraints were measured using the calibrated sensor outputs for an 8 mm flyby through the calibration area, shown in Fig. 7. The errors in  $g_y$  and, to a lesser extent,  $g_p$  vary systematically with tooth pitch, indicating unmodeled platen sensor errors. However, the  $g_x$  error varies gradually over multiple pitches, suggesting unmodeled coordination sensor effects.

The laser interferometer was again sampled to provide an independent verification for a fly-by of 8 mm, while simultaneously sampling the platen sensor and coordination sensor outputs. The platen sensor position error (using the interferometer as ground truth) decreased from  $7.3 \mu\text{m}$  uncalibrated to  $4.4 \mu\text{m}$  using the initial parameters from the separate calibrations to  $2.9 \mu\text{m}$  for the final calibration, a significant improvement. The error of  $\theta_y$  (using the moving sensor segment pair) decreased from  $1.4 \text{ mrad}$  uncalibrated to  $0.40 \text{ mrad}$  for

<sup>4</sup>The `fminu` function in Mathworks Inc.'s Optimization Toolbox for Matlab.



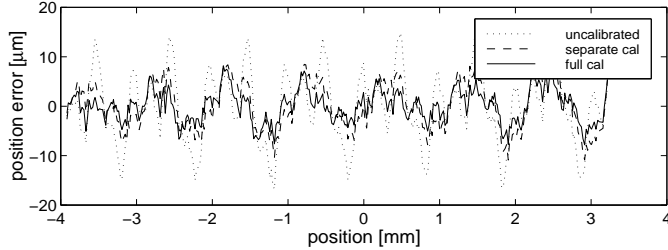


Figure 8. Position error in direction of motion during motion through dual sensor calibration region.

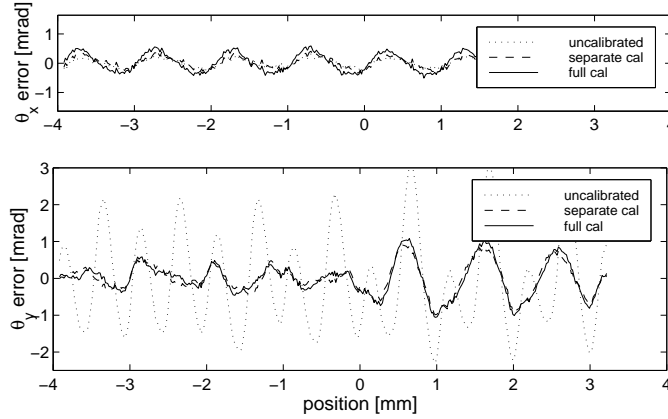


Figure 9. Angle error during motion through dual sensor calibration region.

the separate calibration, but increased slightly to 0.43 mrad for the combined calibration. The error of  $\theta_x$  (using the nominally stationary sensor segment pair), which was expected to decrease when adding the lateral platen sensor parameters, remained small but increased from 0.13 mrad uncalibrated to 0.17 mrad for the separate calibration to 0.30 mrad for the combined calibration. In addition, the identified values of the  $k_{i,9}$ ,  $k_{i,10}$  parameters were all under  $2 \mu\text{m}$ , which were smaller than the lateral effects seen in previous data, strongly suggesting that these less significant parameters are not being correctly identified.

#### 4. Conclusions

Experiments showing the autonomous calibration of the two planar robot sensors demonstrated a marked improvement in accuracy by a factor of three, to a level of  $3 \mu\text{m}$  in translation and 0.4 mrad in rotation, a level of accuracy comparable to results of an interferometer-based calibration [3]. However, these values are significantly higher than the  $0.2 \mu\text{m}$  sensor resolutions. Two effects are limiting further accuracy improvements. First, the platen teeth are assumed to be uniform, but actually have significant manufacturing deviations. Using interferometer position measurement errors of the platen sensor over a

series of seven teeth to compute an average sensor error waveform gave an error from platen tooth variations of  $1.9 \mu\text{m}$ . Further accuracy improvements would require a global model of the platen or more uniform platens – which are currently under development in our laboratory. The second limitation is from unmodeled nonlinearities in the coordination sensor. Although the experiments were designed to keep the coordination sensor angles small, it was necessary to move several pitches for identifiability reasons, and even this small motion seems to have produced errors of several microns, as shown in the  $g_x$  error in Fig. 7.

We intend to calibrate the internal coordination sensor parameters and re-attempt identification of the lateral effect parameters of the platen sensor. In addition, we are currently applying the autonomous calibration technique to calibrate the force output of the redundant planar linear motor actuators. Preliminary results indicate improvements in both force ripple and linearity. Finally, we are integrating the improved models into the closed-loop controllers, enabling improved high-performance operations.

## Acknowledgements

We wish to thank Ralph Hollis, Zack Butler, Michael Chen, and Jimmy Ma for their contributions. This work is supported in part by NSF grants DMI-9523156 and DMI-9527190. Quaid is supported by a Lucent Technologies fellowship.

## References

- [1] A. A. Rizzi, J. Gowdy, and R. L. Hollis, “Agile Assembly Architecture: an agent based approach to modular precision assembly systems,” in *Proc. IEEE Int’l Conf. on Robotics and Automation*, pp. 1511–1516, April 1997.
- [2] E. R. Pelta, “Two-axis Sawyer motor for motion systems,” *IEEE Control Systems magazine*, pp. 20–24, October 1987.
- [3] Z. J. Butler, A. A. Rizzi, and R. L. Hollis, “Integrated precision 3-DOF position sensor for planar linear motors,” in *Proc. IEEE Int’l Conf. on Robotics and Automation*, 1998.
- [4] W.-C. J. Ma, “Precision optical coordination sensor for cooperative 2-DOF robots,” Master’s thesis, Carnegie Mellon University, Pittsburgh, PA, 1998.
- [5] A. E. Quaid, Y. Xu, and R. L. Hollis, “Force characterization and commutation of planar linear motors,” in *Proc. IEEE Int’l Conf. on Robotics and Automation*, pp. 1202–1207, April 1997.
- [6] D. J. Bennett and J. M. Hollerbach, “Autonomous calibration of single-loop closed kinematic chains formed by manipulators with passive endpoint constraints,” *IEEE Transactions on Robotics and Automation*, vol. 7, no. 5, pp. 597–606, 1991.
- [7] J. M. Hollerbach and D. M. Lokhurst, “Closed-loop kinematic calibration of the RSI 6-DOF hand controller,” in *Proc. IEEE Int’l Conf. on Robotics and Automation*, (Atlanta, GA), pp. 142–148, May 1993.
- [8] R. M. Voyles and P. K. Khosla, “Collaborative calibration: Extending shape from motion calibration,” in *Proc. IEEE Int’l Conf. on Robotics and Automation*, (Albuquerque, NM), pp. 2795–2800, April 1997.